

Cite this: *Nanoscale*, 2017, 9, 16437

Real-time visualization and sub-diffraction limit localization of nanometer-scale pore formation by dielectric breakdown†

Adam Zrehen, Tal Gilboa and Amit Meller *

Herein, we introduce synchronous, real-time, electro-optical monitoring of nanopore formation by DB. Using the same principle as sub-diffraction microscopy, our nanopore localization platform based on wide-field microscopy and calcium indicators provides nanoscale sensitivity. This enables us to establish critical limitations of the fabrication process and improve its reliability. In particular, we find that under certain conditions, multiple nanopores may form and that nanopores may preferentially localize at the membrane junction, either of which potentially render nanopore sensing ineffective. As the breakdown parameters of silicon materials are highly manufacturer-specific, we anticipate that our visualization platform will enable users to easily optimize DB fabrication according to specific needs. Furthermore, our technique furthers the applicability of DB to more complicated architectures, such as membranes with selectively thinned regions and plasmonic nanowells.

Received 12th April 2017,
Accepted 27th September 2017

DOI: 10.1039/c7nr02629c

rsc.li/nanoscale

Introduction

Solid-state nanopores show great promise for label-free, single-molecule analyses of biomolecules, including RNAs, proteins, and DNA-protein complexes, as well as for DNA sequencing and genotyping.^{1–8} The method fundamentally involves electrophoretic focusing and threading of charged biomolecules through a single nanometer-scale pore formed in an ultra-thin, insulating membrane while monitoring the ion current flowing through the nanopore used as the principal mode to detect analytes. Among the single-molecule techniques available today, nanopores stand out in their conceptual simplicity and compatibility with label-free detection. Nanopore sensing, however, requires a precise and reproducible means for fabricating the nanometer scale feature in the material of choice. Until recently, the only viable techniques for producing nanopores with dimensional control at the 1 nm scale required either a high-resolution transmission electron microscope (TEM) or a focused ion beam including a helium ion micro-

scope (HIM).^{9–13} These high-cost tools restrict access to the field, limit productivity, and are not optimally suited for large-scale nanopore device manufacturing.

With the rapid and sharp growth in nanopore-based single molecule studies in the past few years, alternative methods for precise nanopore fabrication have been in demand. A particularly attractive approach presented by Kwok *et al.* circumvented the need for any highly specialized equipment entirely and offered numerous additional advantages.¹⁴ Known as controlled breakdown (CBD), the method relies on the dielectric breakdown (DB) of unprocessed silicon nitride/oxide membranes directly in electrolyte solution by the careful application of 0.4–1 V nm^{−1} transmembrane potentials. The probabilistic production of a nanopore by DB is shown to follow a Weibull distribution^{15–17} with a time-to-breakdown typically on the order of several hundred seconds. While the technique is not only faster than TEM-drilling, it is achieved using a low-cost and broadly accessible voltage/current amplifier and standard DAQ hardware. Furthermore, it requires little user intervention once breakdown parameters are experimentally established.

As aqueous phase DB remains largely unexplored, our understanding of the nanopore formation process is based primarily on studies of dry dielectric breakdown, which are likely to be substantially different due to the large difference in air and water dielectric constants, the presence of free ions in water, *etc.*^{15,18} Moreover, due to the immense difficulty in locating and accurately identifying a nanometric feature in a micron-scale membrane using high resolution electron microscopy, studies of nanopore fabrication by DB have been

Department of Biomedical Engineering, The Technion – Israel Institute of Technology, Haifa, 32000, Israel. E-mail: ameller@technion.ac.il

† Electronic supplementary information (ESI) available: Circuit configuration for voltage/current amplifier; pulse-voltage thresholding scheme for DB determination; example translocation experiment with sample events and dwell time/current blockage analysis; images and raw pulse-voltage data for DB experiments leading to multiple pores; images and raw pulse-voltage data for ambiguous DB events; additional images of pores formed in membranes with selectively thinned regions. See DOI: 10.1039/c7nr02629c

considerably restricted, relying primarily on indirect characterization with molecular rulers and sparse, non-real-time, TEM images.^{14,19} Consequently, a number of important questions about the process have yet to be addressed, limiting our ability to further optimize nanopore formation using DB, and more importantly, restricting the broad usage of the method in biomedical applications.

While nanopore formation by DB shows promise as an alternative highly accessible nanopore fabrication method, two main outstanding challenges currently limit its wide scale usage: first, it has so far been widely assumed that nanopore fabrication techniques based on DB consistently lead to the formation of a single nanopore. Given the stochastic nature of nanopore fabrication, it would seem unlikely that multiple nanopores would form simultaneously for experiments lasting several hundred seconds. However, under conditions of low pH and/or high voltage¹⁴ for speeding up breakdown, and for thin (<10 nm) membranes,^{14,20} pore fabrication becomes prohibitively fast (e.g. <10 seconds) to rule out the formation of multiple pores. This is especially problematic given that several hundred milliseconds to several seconds may elapse between the initial pore formation and voltage termination depending on the breakdown technique used. Furthermore, as fabricated pores are then typically expanded by voltage pulses,²¹ albeit at lower values, it is uncertain what the effect of lengthy expansion cycles might have on membranes already exposed to high electric fields. Additional exposure could foreseeably lead to the generation of additional pores. Notably, the ion current by itself cannot distinguish between a single or multiple pores having the same total conductance; however, the unintentional formation of multiple pores may render nanopore sensing ineffective as quantitative electrical sensing in nanopores critically relies on this information.

A second issue is the precise localization of the nanopore in solid-state membranes. It has been taken for granted that nanopores are formed in a random, accessible manner and do not necessarily preferentially form at the membrane junction (edges or corners where alleviated membrane stress exists naturally), where translocations of specifically large biomolecules (e.g. several kbp-long DNA or proteins) may be inhibited by volume constriction²² or attractive/repulsive surface effects.²³ Furthermore, for applications where nanopore localization is desirable, for example electro-optical sensing,^{24,25} time-consuming, specialized scanning procedures had to be implemented^{26,27} for determining the pore location, precluding the use of controlled DB for nanopore fabrication.

In this paper, we introduce synchronous, real-time, electro-optical detection of nanopore formation by DB employing custom wide-field fluorescence microscopy and calcium indicators.^{28,29} The method is straightforward and provides a clear picture of the entire membrane, allowing us to unequivocally address a number of open questions about the fabrication process with sufficient statistics. Specifically, by imaging the nanoscale pore formation moment, we find that multiple nanopores may be generated under certain conditions and that nanopores may preferentially form at certain weak spots.

Additionally, by directly correlating the electrical and optical signal, we are able to accurately discriminate ambiguous DB events, which might appear as transient current spikes,³⁰ initial defects,³¹ or temporary soft breakdown conductive paths.^{16,17,32} Therefore, our method is capable not only of shedding light on some of the past observations referred to above, but furthermore be used to significantly improve the DB technique and increase its usability.

Our visualization technique also enables us to extend the nanopore localization strategy introduced by Carlsen *et al.* based on selectively thinning membranes by helium ion milling (HIM).³⁰ In their work, in order to confirm localization at different breakdown voltages and for different architectures, the membranes were meticulously examined by TEM off-line under vacuum to locate the nanopore. By instead optically monitoring DB in real-time, we are able to rapidly confirm localization to the thinned regions for a large data set. Moreover, our thin region membranes are mass manufactured by wafer-scale UV photolithography rather than milling, which is both time-consuming and laborious since thinning is sequential and requires significant ion dosage calibration.³³ Such architectures are particularly useful for electro-optical sensing.²⁵

Finally, we optically validate our own improved pulse-voltage DB strategy, an extension of multilevel pulse voltage-injection (MPVI).³⁴ At a high applied voltage, the trap-assisted tunneling current (I_{TAT}) dominates over the ohmic contribution (I_{NP}) through the nanopore, where $I_{\text{TOTAL}} = I_{\text{TAT}} + I_{\text{NP}}$, such that I_{NP} cannot be reliably measured. As I_{NP} is unknown at a high voltage, a uniform threshold current to signal pore creation cannot be set, and thus a small target size nanopore cannot be achieved. Although further CBD studies have shown that sub-2 nm nanopores (an average of 1.3 nm) can be produced at a high yield by carefully setting the threshold current,³⁵ we have found that our modified pulse-voltage strategy, as confirmed by direct optical sensing, is able to circumvent the challenges of threshold prediction while recovering the time loss incurred by the monitoring periods of the pulsing approach.

Results and discussion

Optical sensing platform

To optically locate nanopores, we take advantage of the strong, localized nanoscale signal generated by calcium indicators, as previously utilized for an optical nanopore sensing application.^{28,29,36} As demonstrated by numerical simulations and confirmed experimentally, when Ca^{2+} is added to the *cis* chamber and the pore is electrically biased with a negative potential in the *trans* chamber, Ca^{2+} is electrophoretically driven through the pore, resulting in a highly localized accumulation of Ca^{2+} at the nanopore aperture (in the *trans* side), which steeply decreases away from the pore.²⁸ This Ca^{2+} gradient amplitude and scale can be fine-tuned in three ways: (i) by altering the bulk concentration of Ca^{2+} , (ii) by adjusting

the applied electric potential, or (iii) by adding a *trans*-side Ca^{2+} chelator such as EGTA. When an indicator dye (e.g. Fluo-4) is present in the *trans* chamber, it binds to Ca^{2+} and releases a strong fluorescent signal commensurate to the local Ca^{2+} concentration. Consequently, the fluorescence intensity is strongest at the pore opening and radially declines to a low background level, such that the location of the nanopore can be precisely pinpointed (Fig. 1b). Interestingly, we note that while this fluorescence spot can be substantially smaller than the optical point spread function (PSF), defined by $\lambda/(2\text{NA})$ where λ is the light wavelength and NA is the microscope objective numerical aperture, its location in 2D can be determined to an arbitrary precision using the same principle as super-resolution localization microscopy.^{37,38} Hence, in principle, our optical imaging technique allows us to localize the DB pore formed at nanoscale precision, without the help of an electron microscope.

To achieve real-time optical monitoring of the DB process when the location of the nanopore is yet unknown, the entire membrane ($<60 \times 60 \mu\text{m}^2$) must be illuminated and the fluorophores laser-excited at the appropriate wavelength. To this end, we use a wide-field microscope that provides a roughly

$135 \times 80 \mu\text{m}^2$ viewable area and expand the laser beam using a custom telescope. The chips are mounted in CTFE cells as shown in Fig. 1a. In order to preserve the DB kinetics, we calibrate the laser intensity, CaCl_2 concentration (50 mM), and Fluo-4 concentration (0.1–20 nM) to obtain the minimal detectable fluorescent signal above the background ($\text{SNR} > 3$). We use the same strategy for localizing nanopores that are drilled and imaged separately. For these experiments, the concentration of CaCl_2 and Fluo-4 are maintained high at 500 mM and 500 nM, respectively, and 10 mM EGTA is added. We note that bleached fluorophores in the excitation volume are constantly diffusion-replenished from the bulk, permitting very long experiments (at least 25 minutes).

Real-time electro-optical monitoring of DB

Fig. 2 and Movie S1† show an example of DB optically monitored in real time (see the Methods section for our modified pulse-voltage strategy). The breakdown event occurs at 459.4 ± 0.1 s (pulse B) and is identifiable in two ways: (i) a jump in current, $\Delta I_1 \sim 200$ pA, of the capacitance trace following pulse B relative to the trace following pulse A, and (ii) a sharp increase in the fluorescent signal at pulse B several standard deviations above the basal level. Since the tunnelling current (I_{TAT}) dominates the total current ($I_{\text{TOTAL}} = I_{\text{TAT}} + I_{\text{NP}}$) at a high voltage, the short saturating current (>200 nA) cannot be reliably used to signal pore creation. Conversely, the fluorescent signal, which is a direct measure of the ohmic contribution and contains no I_{TAT} component, perfectly aligns with pulse B, unequivocally signalling pore formation 2–3 seconds before capacitance settling. Note that following pore for-

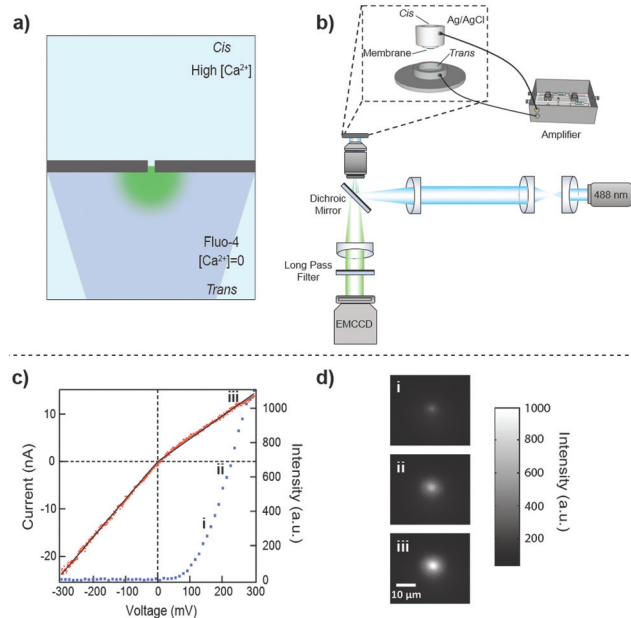


Fig. 1 Principle of real-time electro-optical monitoring of nanopore formation by DB. (a) Illustration (not to scale) of the fluorescent signal that forms at the nanopore *trans* opening as Ca^{2+} ions are driven through by the application of a positive potential. The *trans* side is filled with Ca^{2+} -activated Fluo-4 and illuminated by a 488 nm laser as shown in (b). The resulting signal is filtered by a long-pass filter (cutoff 510 nm) and captured with an EMCCD. (c) Current–voltage (I – V) curve (red markers) showing two linear regimes as expected for an asymmetric electrolyte concentration. The fluorescence intensity (blue markers) increases only with a positive voltage in conjunction with the flow of Ca^{2+} ions into the *trans* chamber to activate Fluo-4. Solid black lines are linear fits to the I – V curves. (d) Images of the fluorescent spots correlating with the intensity curve at positions i–iii.

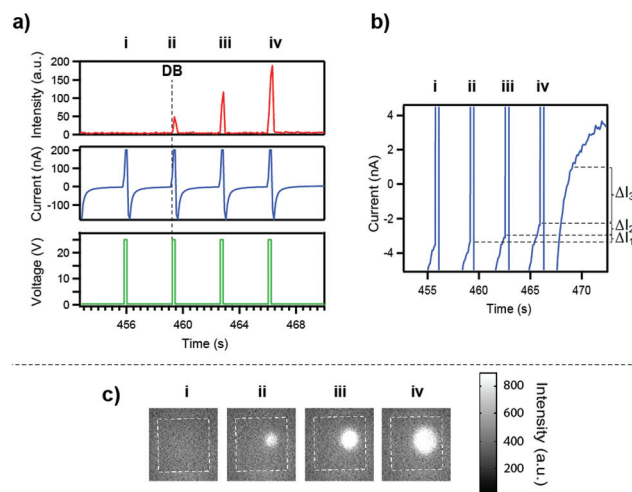


Fig. 2 Real-time synchronous electro-optical monitoring of DB. (a) The membrane is subjected to 25 V 225 ms pulses separated by 3 s monitoring periods at 300 mV. The current saturates at ± 200 nA with each pulse due to the DAQ card range. DB occurs at 459.4 ± 0.1 s in conjunction with an increase in the fluorescence intensity and the formation of a fluorescent spot as shown in (c). The intensity value is a summation of 7×7 pixels (background corrected). A zoom in of the current trace is given in (b), $\Delta I_1 = 200$ pA, $\Delta I_2 = 720$ pA, $\Delta I_3 = 3.57$ nA, where DB occurs at pulse ii. Dotted line represents the membrane boundary.

mation, the fluorescent signal during probing is only slightly higher due to the very low Fluo-4 concentration in the buffer. Instead of dropping the voltage following pore creation as is normally done, we allow the pore to be expanded by up to two additional 25 V pulses to study the effects of continued pulsing, as discussed later. As the electrode offset must be adjusted following the opening up of a low resistance ionic path, the open pore current following formation (in this case ~ 3.5 nA) is somewhat artificial (± 1 nA).

Since the observed fluorescent spot should be a positive function of the Ca^{2+} concentration, we double-check the identity of DB-fabricated nanopores by sweeping the applied transmembrane potential in the range of -300 to 300 mV at a higher Fluo-4 and CaCl_2 concentration (0.5 μM and 500 mM, respectively). As shown in Fig. 1c and Movie S2,[†] at positive voltages, the fluorescence intensity sharply increases as greater numbers of Ca^{2+} ions migrate from *cis* to *trans*. When the electrophoretic force acting on Ca^{2+} is reversed, the fluorescent spot disappears and becomes independent of voltage. As expected, the measured current *versus* the voltage curve shows two different slope regimes correlating with the asymmetric electrolyte distribution: at a negative voltage, the excess *trans* Cl^- ions dissociated from CaCl_2 flow into the *cis* chamber in the direction of the electric and chemical gradient, whereas at a positive voltage, the current is limited since the Cl^- ions must overcome the chemical gradient.

We next validated the functionality of our DB-fabricated nanopores. For this, we added 6 kbp DNA to the *cis* chamber and measured the translocations under different applied voltages. Fig. S3[†] represents the scatter plot of the analysed events. The measured dwell time decreases appreciably with increasing voltage, as expected for fully translocating events and not collisions.³⁹ At 100 mV, primarily non-folded events are observed due to the decreased driving force for translocation. A pore diameter of 4.5 ± 0.8 nm based on the molecular ruler model is consistent with these blockage levels. The conductance model,^{19,40} $G = \sigma[4t/\pi d^2 + 1/d]^{-1}$, with a bulk conductivity, σ , of 10.5 S m^{-1} for 1 M KCl pH 7.5, and a membrane thickness, t , of 20 ± 2 nm, gives a pore size d of 8 ± 0.4 nm. The discrepancy between the molecular ruler and conductance model estimation is likely attributed to pore geometry. Attempts have been made to determine the pore shape⁴¹ and estimate the conductance model measurement error³⁵ for nanopores formed by DB. An effective thickness, t_{eff} , of $1/3t$ similar to TEM-drilled pores^{42,43} is used by Yanagi *et al.*³⁴ for $10+$ nm membranes, whereas $t_{\text{eff}} = t$ is used for <10 nm membranes.²⁰ Taking $t_{\text{eff}} = 6.7 \pm 0.7$ nm instead results in a pore diameter of 5.1 ± 0.2 nm, in agreement with the molecular ruler estimation.

Nanopore localization and mapping

To address the question of where DB nanopores are formed in the membrane, we optically localized numerous DB-fabricated nanopores in two different membrane architectures. In order to compare nanopore localizations from different membranes, we first used transmitted white light microscopy to precisely

measure the size of each and every membrane. The relative location of each nanopore was then defined as a fraction of its x and y position along the membrane dimension. In the first batch of chips (Fig. 3a), both electro-optically monitored as well as electrically monitored nanopores distribute randomly on the membrane, consistent with a uniform membrane thickness or a uniform distribution of defects. However, in the second batch (Fig. 3b), a disproportionate number of nanopores (roughly 20%) fall in very close proximity to the membrane edges, as supported by the Gaussian fitting of the pore location (Fig. 4c), explained later. This may be due to fabrica-

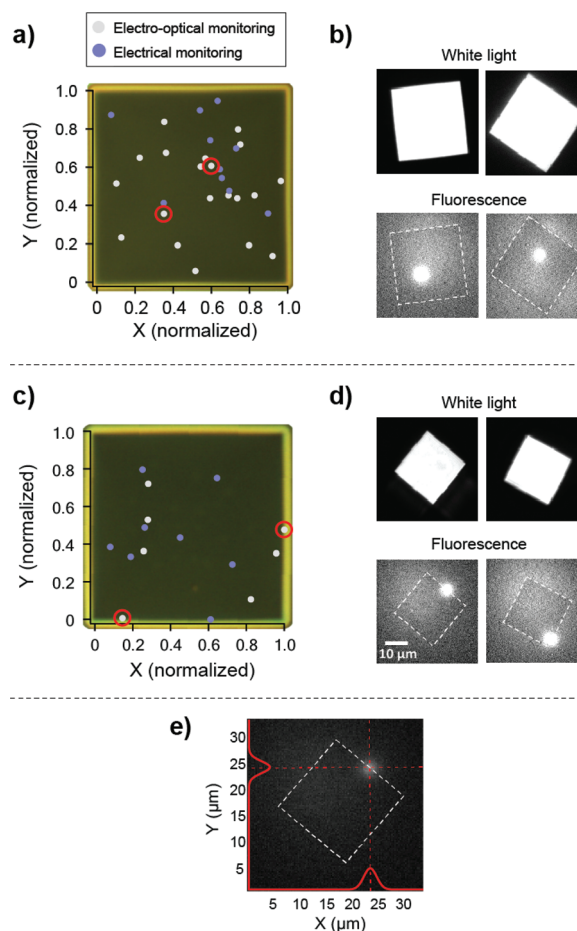


Fig. 3 Mapping of drilled nanopores. (a) Spatial distribution of nanopore location with respect to the membrane boundaries. Localization shown for nanopores drilled with real-time optical monitoring (grey markers, $N = 10$) and without optical monitoring (blue markers, $N = 20$). Nanopores are fabricated in 18 ± 2 nm thick $\sim 32 \times 32$ μm^2 membranes with 25 V 225 ms pulses. Circled dots correspond with the fluorescent spots in (b). (c) Spatial distribution of nanopores with real-time optical monitoring (grey markers, $N = 7$) and without optical monitoring (blue markers, $N = 8$) in 23 ± 2 nm thick $\sim 20 \times 20$ μm^2 membranes with 22.5 V 250 ms pulses. These pores show a higher tendency to form at the edge compared with (a). Raw images of circled points are given in (d). 20% of nanopores ($N = 15$) lie precisely at the membrane edge as confirmed by Gaussian fittings of the corresponding fluorescent spots (e). Fitting results: $x = 23.58$ μm , $y = 24.58$ μm , $\sigma_x = 1.77$ μm , $\sigma_y = 1.68$ μm .

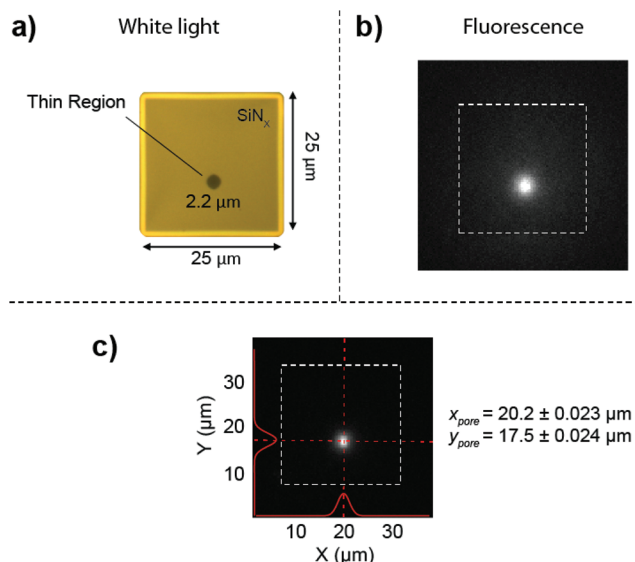


Fig. 4 Directing DB to pre-thinned localized regions and sub-diffraction spatial localization. (a) White light illumination of a $25 \times 25 \mu\text{m}^2$ SiN_x membrane (thickness: $45 \pm 2 \text{ nm}$) in which a $2.2 \mu\text{m}$ in diameter thinned region (thickness: $20 \pm 2 \text{ nm}$) is created using wafer-scale photolithography with a backside alignment. The thin region appears darker when illuminated. (b) The bright fluorescent spot emanating from the thin region corresponds with the nanopore location following DB with 25 V 225 ms pulses. (c) Sub-diffraction localization of the nanopore obtained by 2D Gaussian fitting. In order to optimize the fitting, the exposure time (1 s) and Ca^{2+} concentration (50 mM) were adjusted, and the background (probing at -300 mV) was averaged over 10 frames and subtracted from the signal (probing at 300 mV) averaged over 10 frames. Fitting results: $x = 20.2 \pm 0.023 \mu\text{m}$, $y = 17.5 \pm 0.024 \mu\text{m}$, $\sigma_x = 1.50 \mu\text{m}$, $\sigma_y = 1.60 \mu\text{m}$.

tion effects or a local enhancement of the transmembrane potential applied for DB. Importantly, such nanopore positioning could inhibit or alter the translocation dynamics of large biomolecules such as kbp-long DNA with radius of gyrations in the hundreds of nanometers range (e.g. 9 kbp–300 nm)⁴⁴ due to the increased entropic barrier, similar to observations of DNA trapped in nanostructure openings.²²

As we have demonstrated, nanopores fabricated by DB typically distribute randomly on a membrane of uniform thickness. We next evaluated the possibility of directing DB nanopore formation to lithography defined pre-thinned regions in the SiN_x membrane. Our nanopore devices are prepared by two-step photolithography as described previously (see the Methods section). Fig. 4 shows an example of an imaged nanopore fabricated by DB in a $\sim 45 \text{ nm}$ thick membrane containing a $\sim 20 \text{ nm}$ thinned region, $\sim 2.2 \mu\text{m}$ in diameter ($<0.5\%$ of the total surface area). Pore formation was optically monitored in real time and then the buffer was swapped with higher concentrations of Fluo-4 and Ca^{2+} to enhance the signal. As can be seen, the pore landed in the thinned region.

We have observed thickness-dependent pore localization in 100% ($N = 34$) of cases for a variety of membrane architectures, as detailed in the Methods section. Additional examples are

given in Fig. S9.† These results highlight the strong dependence of breakdown on the trap-assisted electron tunneling⁴⁵ cross-section. Despite an overwhelmingly larger global membrane surface area with a greater total number of charge traps, the probability of forming a connected path of traps that span the thicker membrane is evidently negligible. Although the behavior may be less predictable for other architectures and materials, clearly, wafer-scale manufacturing of thin region membranes for specialized applications is a real possibility.

Using sub-diffraction limit localization, we are able to precisely locate the center position of the nanopore inside the circular thin region wells. Although our primary aim was to find rather than to direct the nanopore with nanoscale sensitivity, which could be achieved by reducing the surface area of the thin regions, this localization measurement is nonetheless critical for future nanopore applications. For example, some nanopore sequencing methods rely on the embedment of nanoscale electrodes for transverse electrical measurements, necessitating the confirmation of pores at this junction.^{46,47,48} For all drilled pores, a 2D Gaussian function was fitted using a non-linear least squares algorithm (Fig. 3e and 4c). This fitting yielded the center of the Gaussian, representing the nanopore location and the standard deviation in x and y .

To determine the best possible accuracy obtainable using this fitting, we optimized the experimental conditions. Specifically, the exposure time was increased to 1 s to obtain a higher photon count, the concentration of Ca^{2+} was reduced to 50 mM to shrink the Ca^{2+} gradient, and the focus was fine-tuned relative to the fluorescent spot. The background (probing at -300 mV) was averaged over 10 frames and subtracted from the signal (probing at 300 mV) averaged over 10 frames. A 2D Gaussian function was then fitted to this background-subtracted image, and the total number of photons was computed by correlating the electron count and photon count according to the camera specifications (e.g. gain, quantum efficiency, etc.) Based on these parameters, the fitting accuracy in x and y was determined.³⁸ For the nanopore represented in Fig. 4, we achieved sub-diffraction limit accuracy (45 and 48 nm uncertainty in x and y , respectively), demonstrating the power of our optical platform.

Extending the principle of thickness-dependent pore localization, we also examined the possibility of forming nanopores in plasmonic nanowells, which have been shown to significantly suppress background light and enhance fluorescence.⁴⁹ In this architecture, the SiN_x membrane is uniform in thickness, yet it is overlaid almost entirely with 130 nm polycrystalline gold, except at 5×5 120 nm in diameter circular regions. As DB has been shown to act on gold-coated SiN_x ,⁵⁰ we needed to confirm that nanopores would form within the nanowells themselves. Indeed, as illustrated in Fig. S10,† nanopores fabricated by DB fall in the nanowells instead of elsewhere in the metallized membrane.

Multiple pore formation

As mentioned earlier, in order to evaluate the threshold and parameter (voltage, pulse time) sensitivity of DB fabrication,

we allow the high voltage pulses to continue another 2–3 cycles following pore formation before switching to a low probing voltage. In the first batch, we observed the formation of multiple pores in both electrically monitored and electro-optically monitored drilling experiments in as much as 20% ($N = 40$), with two examples showing more than one pore forming simultaneously (see Fig. S4†). As shown in Fig. 5, the first pore forms at around 389 seconds, as signaled by a jump in fluorescence and a change in the final 150 ms of the capacitance trace of roughly 300 pA. An additional high voltage pulse expands the pore moderately as reflected by the increase in fluorescence signal and current change (~ 350 pA). The next pulse results in a noticeably larger current change relative to the previous (~ 1.05 nA), in conjunction with the opening up of another pore. Interestingly, the second pore forms following only an additional ~ 225 ms of exposure to the high electric

field, or 0.57% of the total experiment exposure, and despite the rerouting of the electric charge through the newly formed ion gateway. In relation to the Weibull distribution for dry DB, which is qualitatively similar to the aqueous case,^{15,18} such sharp breakdown transitions are consistent with a large Weibull slope, β .^{15,17} Additional examples are given in Fig. S4 and S5.†

The fairly high likelihood of multiple pores forming within ~ 200 – 400 ms of one another observed for this batch highlights the importance of setting the appropriate breakdown parameters, in particular the pulse duration relative to the magnitude of the voltage pulse. In the MPVI method, the pulse duration is set to continuously increase (exceeding 1 s at a 90% pore formation likelihood), and $\sim 60\%$ of pores are shown to form in <1 s of total high voltage exposure.³⁴ In the CBD method, several seconds may elapse between pore creation and voltage cut-off, which is allotted for pore growth.¹⁴ As the Weibull distribution (time-to-pore formation) shrinks with increasing applied voltage, extreme pH, and decreasing membrane thickness,¹⁴ the probability of forming multiple pores within short intervals of one another increases. As we show, real-time electro-optical monitoring can be used to calibrate the DB design to ensure the efficient production of a single nanopore.

For massive parallelization applications where multiple nanopores on a single membrane are desirable, we fabricated chips with an array of 3×3 to 6×6 wells and attempted to drill multiple pores. Examples are given in Fig. S6 and Movie S3.† Our results showed two concurrent phenomena: the emergence of multiple pores (up to 6) in different wells, and the coincident growth of previous pores, as indicated by an increase in fluorescence. This highlights the potential advantage of our optical platform, which could be coupled with future technologies to enable well-controlled nanopore arrays.⁵¹

Conclusions

In this report, we present a technique for monitoring DB visually in real time, as well as mapping nanopores formed by DB, which is substantially simpler and more effective than TEM imaging. Real-time, wide-field optical monitoring of DB nanopore formation revealed that multiple pores can form, which was overlooked by previous studies relying exclusively on electrical readout. Moreover, the optical images allow us to identify pore formation at membrane edges, which can hinder biomolecule capture and translocation. Breakdown parameters are highly batch-specific, dependent not only on the membrane thickness, composition, and surface area, but also on the material configuration and chip manufacturing process, which is in agreement with the observations of other studies.¹⁵ In particular, SiN_x deposition may vary significantly among producers, imparting different structural properties to prepared membranes and thus different trap generation rates⁵² under an applied voltage. Thus, nanopore quality control is

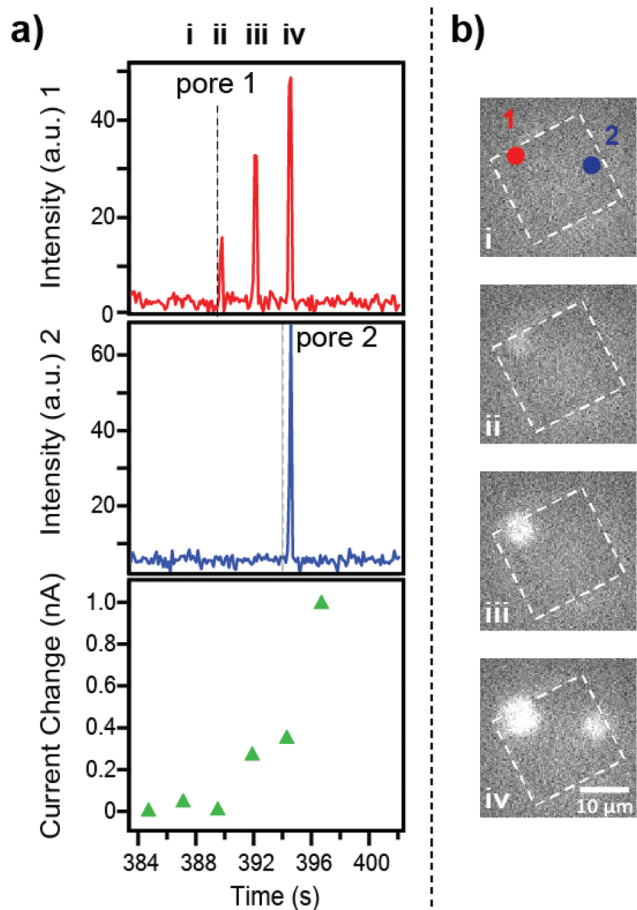


Fig. 5 Synchronous electro-optical monitoring of DB resulting in the formation of two nanopores. (a) The membrane is subjected to 25 V 225 ms pulses separated by 2 s monitoring periods at 300 mV. The first pore forms at pulse ii, shown as an increase in the fluorescence intensity and an abrupt rise in current between the final 150 ms of the capacitance curves of successive pulses (see Fig. S2† for the detailed pulse-voltage strategy), which is offset 2 s from the fluorescent signal. A second nanopore forms after an additional ~ 225 ms of high voltage exposure. The intensity value is a summation of 7×7 pixels (background corrected). (b) Raw images of pore formation at two locations.

inherently limited by the variability of manufacturing and cannot necessarily depend on literature values. It is therefore essential to be able to efficiently locate DB-fabricated pores and monitor fabrication in real-time in order to determine the ideal set of production conditions, as an initial one-time calibration.

As previously reported,^{15,28} the characteristic current jump indicative of DB, which may initially result in a non-zero “open pore” current at a low probing voltage, sharply or slowly declines to a negligible or significantly lower value relative to the initial few seconds following breakdown (see Fig. S7 and S8†). This leads to doubt as to whether a successful breakdown event has occurred. With an optical monitoring platform, however, these ambiguous events as well as initial defects in low capacitance devices³¹ can be quickly discriminated.

Our rapid nanopore visualization strategy also advances the applicability of DB for more complicated architectures, where the nanopore location relative to pre-existing features must be verified.^{46–48} In particular, optical nanopore experiments rely on direct measurements of photon emission at the pore vicinity. Thus, it is critical that the position of the nanopore be known or readily identifiable. Herein, we optically validated nanopore localization to thinned membrane regions, to micro-well arrays and to gold nanowells.⁵³ We anticipate that the imaging platform presented here can be used in the development and optimization of a variety of other electrochemical nanopore fabrication techniques in emerging alternative materials, such as graphene and hBN. Given the inherent low-noise localized properties of the fluorescent signal at pore creation,²³ it is foreseeable that real-time ultrafast optical monitoring could provide more precise nanopore size control in future studies.

Methods

Chip fabrication

Nanopore chips were fabricated from a 4 inch silicon wafer coated with SiO₂ (500 nm) and low-stress amorphous silicon nitride (SiN_x, 50 nm). Certain SiN_x membranes were additionally thinned to 20–25 nm by reactive ion etching (RIE) at a CF₄ (g) to O₂ (g) ratio of 9:1 or by wet etching with BOE. Membranes with locally thinned regions 15–22 nm in thickness were prepared by an initial backside alignment step before opening up the membrane by KOH etching as described previously.⁴⁹ These include (i) $\sim 40 \times 40 \mu\text{m}^2$ membranes containing a single $\sim 3.7 \mu\text{m}$ thinned region, (ii) $\sim 49 \times 49 \mu\text{m}^2$ membranes containing a single $\sim 3.4 \mu\text{m}$ thinned region, (iii) $\sim 25 \times 25 \mu\text{m}^2$ membranes containing a single $\sim 2.2 \mu\text{m}$ thinned region, and (iv) $\sim 56 \times 56 \mu\text{m}^2$ membranes containing a 3×3 to 6×6 array of $\sim 1.5 \mu\text{m}$ thinned regions.

Controlling DB

An in-house voltage/current amplifier and custom LabVIEW software were used to control breakdown (Fig. S1†). We have found that a voltage-pulse strategy similar to that employed by

Yanagi *et al.* (MPVI)³⁴ is best suited to our custom-made chips because, upon application of a high constant voltage, the large capacitance current (in the range of 100s of nA) that follows makes it challenging to control breakdown and detect pore creation. Furthermore, we have found that for several batches, the time it takes for the capacitance current to settle to negligible sub-pA levels during the monitoring periods between voltage pulses is extremely long: for example, in some cases it takes tens of seconds for the capacitance current to fully settle. Thus, to accelerate the time-to-pore-formation, our method caps the monitoring period at 2–3 seconds, much before the capacitance settles, and instead examines the capacitance trace to determine whether a pore has been formed, using the following procedure (Fig. S2†):

The first, more sensitive threshold for pore creation is based on a comparison of the final 100–150 ms of a 2–3 s capacitance trace before and after a voltage pulse. If a minimum rise of 200 pA is detected, then pore creation is signalled, and pulsing at a high voltage is stopped. As confirmed by real-time optical measurements, even though our method bypasses capacitance settling, we can accurately predict pore formation since any changes in the steady state monitoring period must be attributed to a change in membrane resistance, *i.e.* pore creation. As occasionally pore formation is much more gradual, growing at <200 pA per iteration, a second threshold is set at a fixed current level, *e.g.* 2 nA or higher depending on the application. We note that typical changes of a few nA are observed between the initial few pulses of an experiment, which may be due to shifting electrode potentials or changes in the membrane surface charge. Therefore, the thresholding algorithm is only activated once the system reaches steady state, and usually 5–10 V pulses are applied before ramping up to 20–25 V.

Electro-optical measurement system

Chips were cleaned by exposing them to 50% oxygen plasma for 30 s prior to use. The chips were then mounted on custom CTFE cells with Ecoflex 5 (Smooth-ON) silicone rubber to separate the *trans* and *cis* sides of the membrane. Next, 1 M KCl, 40 mM Tris-HCl, and 1 mM EDTA were added to both chambers. For pre-DB drilled experiments, 10 mM EGTA and 500 nM Fluo-4 were added to the *trans* chamber and 50–500 mM CaCl₂ was added to the *cis* chamber. For electro-optical DB experiments, 0.1–20 nM Fluo-4 was added to the *trans* chamber and 50 mM CaCl₂ was added to the *cis* chamber.

For optical sensing, a custom wide field microscope was constructed. Briefly, one collimated 488 nm laser (iFlex-Viper, PointSource) coupled through a single-mode polarization-preserving optical fiber is focused on a high NA objective (Olympus Plan Apochromat 60 \times /1.45) and expanded to illuminate the membrane position at an average intensity of $2 \mu\text{W} \mu\text{m}^{-2}$ at the image plane. The emitted light is collected by the same objective and focused onto an EMCCD camera (Andor iXon 887). For experiments where the pore was first drilled and then imaged, the ion current flowing through the pore was

measured using two Ag/AgCl electrodes connected to a high bandwidth amplifier (Axon 200B) and filtered at 100 kHz. For electro-optical DB experiments, the electrodes were connected to a custom voltage/current amplifier and filtered externally (Krohn-Hite 3202) at 10 Hz. For data acquisition, we used two DAQ boards: NI-PCI-6052E for the analog, electrical signal and NI-PCI-MIO-16E-1 for recording the fire pulses of the camera (thus providing exact timing of each camera frame). The two cards were triggered simultaneously, shared the same 250 kHz sampling clock *via* a hardware connection, and were fully controlled by a custom LabVIEW program, to allow high accuracy synchronization between the camera and the ionic signal. Images were taken at 0.1–1 s exposure.

Translocation experiments

Pores fabricated by DB were probed at a low voltage (0.1 to 0.3 V) for 20+ minutes or left in 3.6 M LiCl pH 10 for several hours to obtain a stable open pore current prior to adding 6 kbp NoLimits DNA (Fischer Scientific). Events were monitored using an Axon 200B filtered at 100 kHz and custom LabVIEW software.

Conflicts of interest

The authors declare no competing financial interest.

Acknowledgements

We are grateful to A. Girsault for his assistance in image processing. Fabrication and characterization of the devices were performed at the Technion MNF & PU facilities. We acknowledge financial support from the BeyondSeq consortium (EC program 63489) and the i-Core program of the Israel Science Foundation (1902/12).

References

- 1 D. Branton, D. W. Deamer, A. Marziali, H. Bayley, S. A. Benner, T. Butler, M. Di Ventra, S. Garaj, A. Hibbs, X. Huang, S. B. Jovanovich, P. S. Krstic, S. Lindsay, X. S. Ling, C. H. Mastrangelo, A. Meller, J. S. Oliver, Y. V. Pershin, J. M. Ramsey, R. Riehn, G. V. Soni, V. Tabard-Cossa, M. Wanunu, M. Wiggin and J. A. Schloss, *Nat. Biotechnol.*, 2008, **26**, 1146.
- 2 C. Dekker, *Nat. Nanotechnol.*, 2007, **2**, 209.
- 3 M. Wanunu, *Phys. Life Rev.*, 2012, **9**, 125.
- 4 R. Wei, V. Gatterdam, R. Wieneke, R. Tampé and U. Rant, *Nat. Nanotechnol.*, 2012, **7**, 257.
- 5 M. Langecker, A. Ivankin, S. Carson, S. R. M. Kinney, F. C. Simmel and M. Wanunu, *Nano Lett.*, 2015, **15**, 783.
- 6 I. Nir, D. Huttner and A. Meller, *Biophys. J.*, 2015, **108**, 2340.
- 7 A. Squires, E. Atas and A. Meller, *Sci. Rep.*, 2015, **5**, 11643.
- 8 E. C. Yusko, B. R. Bruhn, O. Eggenberger, J. Houghtaling, C. Ryan, N. C. Walsh, S. Nandivada, M. Pindrus and A. R. Hall, *Nat. Nanotechnol.*, 2017, **12**, 360.
- 9 M. J. Kim, M. Wanunu, D. C. Bell and A. Meller, *Adv. Mater.*, 2006, **18**, 3149.
- 10 M. J. Kim, B. McNally, K. Murata and A. Meller, *Nanotechnology*, 2007, **18**, 205302.
- 11 J. Yang, D. C. Ferranti, L. A. Stern, C. A. Sanford, J. Huang, Z. Ren, L.-C. Qin and A. R. Hall, *Nanotechnology*, 2011, **22**, 285310.
- 12 C. J. Lo, T. Aref and A. Bezryadin, *Nanotechnology*, 2006, **17**, 3264.
- 13 A. J. Storm, J. H. Chen, X. S. Ling, H. W. Zandbergen and C. Dekker, *Nat. Mater.*, 2003, **2**, 537.
- 14 H. Kwok, K. Briggs and V. Tabard-Cossa, *PLoS One*, 2014, **9**, DOI: 10.1371/journal.pone.0092880.
- 15 K. Briggs, M. Charron, H. Kwok, T. Le, S. Chahal, J. Bustamante, M. Waugh and V. Tabard-Cossa, *Nanotechnology*, 2015, **26**, 084004.
- 16 S. Lombardo, J. H. Stathis, B. P. Linder, K. L. Pey, F. Palumbo and C. H. Tung, *J. Appl. Phys.*, 2005, **98**, 121301.
- 17 R. Degraeve, G. Groeseneken, R. Bellens, J. L. Ogier, M. Depas, P. J. Roussel and H. E. Maes, *IEEE Trans. Electron Devices*, 1998, **45**, 904.
- 18 S. Ikonopisov and N. Elenkov, *J. Electroanal. Chem.*, 1978, **88**, 417.
- 19 S. W. Kowalczyk, A. Y. Grosberg, Y. Rabin and C. Dekker, *Nanotechnology*, 2012, **23**, 88002.
- 20 I. Yanagi, K. Fujisaki, H. Hamamura and K. Takeda, *J. Appl. Phys.*, 2017, **121**, 45301.
- 21 E. Beamish, H. Kwok, V. Tabard-Cossa and M. Godin, *Nanotechnology*, 2012, **23**, 0405301.
- 22 W. Reisner, N. B. Larsen, A. Silahtaroglu, A. Kristensen, N. Tommerup, J. O. Tegenfeldt and H. Flyvbjerg, *Proc. Natl. Acad. Sci. U. S. A.*, 2010, **107**, 13294.
- 23 B. N. Anderson, M. Muthukumar and A. Meller, *ACS Nano*, 2013, **7**, 1408.
- 24 B. McNally, A. Singer, Z. Yu, Y. Sun, Z. Weng and A. Meller, *Nano Lett.*, 2010, **10**, 2237.
- 25 T. Gilboa, C. Torfstein, M. Juhasz, A. Grunwald, Y. Ebenstein, E. Weinhold and A. Meller, *ACS Nano*, 2016, **10**, 8861.
- 26 N. Di Fiori, A. Squires, D. Bar, T. Gilboa, T. D. Moustakas and A. Meller, *Nat. Nanotechnol.*, 2013, **8**, 946.
- 27 S. Pud, D. Verschueren, N. Vukovic, C. Plesa, M. P. Jonsson and C. Dekker, *Nano Lett.*, 2015, **15**, 7112.
- 28 B. N. Anderson, O. N. Assad, T. Gilboa, A. H. Squires, D. Bar and A. Meller, *ACS Nano*, 2014, **8**, 11836.
- 29 A. Ivankin, R. Y. Henley, J. Larkin, S. Carson and M. L. Toscano, *ACS Nano*, 2014, **8**, 10774.
- 30 A. T. Carlsen, K. Briggs, A. R. Hall and V. Tabard-Cossa, *Nanotechnology*, 2017, **28**, 085304.
- 31 K. Matsui, I. Yanagi, Y. Goto and K. Takeda, *Sci. Rep.*, 2015, **5**, 17819.

- 32 S. Lombardo, A. La Magna, C. Spinella, C. Gerardi and F. Crupi, *J. Appl. Phys.*, 1999, **86**, 6382.
- 33 A. R. Hall, *Microsc. Microanal.*, 2013, **19**, 740.
- 34 I. Yanagi, R. Akahori, T. Hatano and K. Takeda, *Sci. Rep.*, 2014, **4**, 5000.
- 35 K. Briggs, H. Kwok and V. Tabard-Cossa, *Small*, 2014, **10**, 2077.
- 36 A. J. Heron, J. R. Thompson, B. Cronin, H. Bayley and M. I. Wallace, *J. Am. Chem. Soc.*, 2009, **131**, 1652.
- 37 R. E. Thompson, D. R. Larson and W. W. Webb, *Biophys. J.*, 2002, **82**, 2775.
- 38 K. I. Mortensen, L. S. Churchman, J. A. Spudich and H. Flyvbjerg, *Nat. Methods*, 2010, **7**, 377.
- 39 M. Wanunu, J. Sutin, B. McNally, A. Chow and A. Meller, *Biophys. J.*, 2008, **95**, 4716.
- 40 C. M. Frament and J. R. Dwyer, *J. Phys. Chem. C*, 2012, **116**, 23315.
- 41 C. Ying, Y. Zhang, Y. Feng, D. Zhou, D. Wang, Y. Xiang, W. Zhou, Y. Chen, C. Du and J. Tian, *Appl. Phys. Lett.*, 2016, **109**, 63105.
- 42 M. Wanunu, T. Dadosh, V. Ray, J. Jin, L. McReynolds and M. Drndić, *Nat. Nanotechnol.*, 2010, **5**, 807.
- 43 K. Venta, G. Shemer, M. Puster, J. A. Rodriguez-Manzo, A. Balan, J. K. Rosenstein, K. Shepard and M. Drndić, *ACS Nano*, 2013, **7**, 4629.
- 44 D. E. Smith, T. T. Perkins and S. Chu, *Macromolecules*, 1996, **29**, 1372.
- 45 S. Habermehl, R. T. Apodaca and R. J. Kaplar, *Appl. Phys. Lett.*, 2009, **94**, 12905.
- 46 M. Tsutsui, M. Taniguchi, K. Yokota and T. Kawai, *Nat. Nanotechnol.*, 2010, **5**, 286.
- 47 P. Krishnakumar, B. Gyarmas, W. Song, S. Sen, P. Zhang, P. Krstić and S. Lindsay, *ACS Nano*, 2013, **7**, 10319.
- 48 F. Nicoli, D. Verschuere, M. Klein, C. Dekker and M. P. Jonsson, *Nano Lett.*, 2014, **14**, 6917.
- 49 O. N. Assad, T. Gilboa, J. Spitzberg, M. Juhasz, E. Weinhold and A. Meller, *Adv. Mater.*, 2017, **29**, 1605442.
- 50 H. Kwok, M. Waugh, J. Bustamante, K. Briggs and V. Tabard-Cossa, *Adv. Funct. Mater.*, 2014, **24**, 7745.
- 51 P. Xie, K. Healy and J. Millis, *WO Pat*, 2016187519A1, 2016.
- 52 D. J. DiMaria, E. Cartier and D. Arnold, *J. Appl. Phys.*, 1993, **73**, 3367.
- 53 O. N. Assad, N. Di Fiori, A. H. Squires and A. Meller, *Nano Lett.*, 2014, **15**, 745.